Exploring geometrical stereoscopic aerosol top height retrieval from geostationary satellite imagery in East Asia

Minseok Kim[1], Jhoon Kim[1], Hyunkwang Lim[2], Seoyoung Lee[1], Yeseul Cho[1]

[1]Department of Atmospheric Sciences, Yonsei University, Seoul, 03722, Korea
5 [2]National Institute for Environmental Studies, Tsukuba, Japan

Correspondence to: Jhoon Kim (jkim2@yonsei.ac.kr)

Abstract. Despite the importance of aerosol height information for events such as volcanic eruptions and long-range aerosol transport, spatial coverage of its retrieval is often limited because of a lack of appropriate instruments and algorithms. Especially, geostationary satellite observations provide constant monitoring for such events. This study assessed the application of different viewing geometries for a pair of geostationary imagers to retrieve aerosol top height (ATH) information. The stereoscopic algorithm converts the lofted aerosol layer parallax, calculated using image-matching of two visible images, to ATH. The sensitivity study prospects a reliable result using a pair of Advanced Himawari Imager (AHI) and Advanced Geostationary Radiation Imager (AGRI) images at 40° longitudinal separation. The pair resolved aerosol layers above 1 km altitude over East Asia. In comparison, aerosol layers must be above 3 km to be resolved by paired AHI and Advanced Meteorological Imager (AMI) images at 12.5° longitudinal separation. Case studies indicate that the stereoscopic ATH retrieval results are consistent with aerosol heights determined using extinction profiles from the Cloud–Aerosol Lidar with Orthogonal Polarization (CALIOP). Comparisons between the stereoscopic ATH and the CALIOP height, defined by extinction coefficient data, indicated that 71.3 % of ATH estimates from the AHI and AGRI are within 2 km of CALIOP heights, compared with 49.3 % from the AHI and AMI. The ability of the stereoscopic algorithm to monitor hourly aerosol height variations is demonstrated by comparison with a Korea Aerosol Lidar Observation Network dataset.

1 Introduction

Long-range transboundary transport of aerosols from wildfires and deserts affects air quality over wide areas. Information on aerosol height is crucial in determining the effects of lofted aerosol plumes transported to distant downwind regions. Lidar systems provide detailed vertical profiles of aerosol layers and are primary tools in providing vertically resolved information. 25 Ground-based lidars are capable of high-quality aerosol profiling with little interference from surface signals, and they have been used for long-term analysis of aerosol vertical distributions (Tian et al., 2017; Gupta et al., 2021). However, the requirement for manual management means lidar sites are concentrated in urban areas. Spaceborne lidar instruments such as Cloud–Aerosol Lidar with Orthogonal Polarization (CALIOP; Winker et al., 2013; Wu et al., 2016) provide information on the vertical distributions of aerosol layers worldwide (Kim et al., 2018). Previous studies have used CALIOP observation

30   products to demonstrate seasonal variability in the vertical structures of aerosols over China (Huang et al., 2013; Liao et al., 2021); however, the active sensor has a narrow swath, which means that it sometimes bypasses aerosol transport events. Even if the spaceborne lidar system passes over the aerosol layer, the horizontal variability of the layer outside the swath remains unknown.

Aerosol height retrieval algorithms using passive sensors have been developed to meet the need for a better understanding of

35   aerosol vertical structures over broader areas. Choi et al. (2021) determined information content requirements for passive remote-sensing measurements when profiling aerosols below the planetary boundary layer, using remote sensing of oxygen (O_2)-A and -B bands with higher spectral resolution and polarimetric measurements. For this method, conventional aerosol height retrieval algorithms make use of the absorption bands of O_2, which normally have a stable vertical distribution. Scattered photons travel longer atmospheric paths in aerosol layers at lower altitudes, leading to greater absorption by O_2 and

40   less backscattered radiance being observed in satellite observations. An aerosol height retrieval algorithm using the TROPOspheric Monitoring Instrument (TROPOMI), a hyperspectral spectrometer on-board the Sentinel-5 Precursor (Sentinel-5P), was developed and validated by Nanda et al. (2020), where aerosol height retrieval using TROPOMI utilized hyperspectral observations of the O_2 A band. Aside from the underestimation induced by bright surfaces on land, the results agreed well with CALIOP weighted extinction heights. With additional use of the O_2 B band, Chen et al. (2021) developed

45   an aerosol height retrieval mechanism for TROPOMI for application in surface particulate matter estimation, with the algorithm being applied to absorbing aerosols such as dust and smoke. Additional use of the O_2 B band yields systematically higher (by ~1.6 km) aerosol optical central heights than the TROPOMI operational aerosol height, nearer the height with the strongest backscatter for CALIOP.

Studies have shown that the use of geometrical features of elevated atmospheric structures apparent to multiple sensor

50   imagery is effective, rather than using computationally expensive radiative transfer calculations. Aerosol height retrievals by the Multi-angle Imaging SpectroRadiometer (MISR) Interactive eXplorer (MINX) system make use of multi-angle imagery from nine push-broom cameras on-board the Terra satellite (Nelson et al., 2013). These cameras view 360 km swaths of Earth, with nine viewing angles ranging from nadir to 70.5°. MINX successfully verified aerosol height retrieval using stereoscopic imagery with passive sensors. The synergetic use of two or more sensors for aerosol height retrieval has also

55   been studied (Chu et al., 2008; Lee et al., 2015; Lee et al., 2021). Despite the use of spaceborne passive sensor observations improving the spatial coverage of aerosol vertical structure information, monitoring of diurnal variations in aerosol layers is restricted by the low temporal resolution of low-Earth-orbit (LEO) satellites.

Observation of aerosol vertical structures using geostationary Earth orbit (GEO) satellites has potential for continuously monitoring diurnal variations in aerosol transport over broad areas. For the retrieval of aerosol optical depth (AOD) data, the

60   use of geostationary meteorological satellites such as the Meteorological Imager (MI), Advanced Baseline Imager (ABI), and Advanced Himawari Imager (AHI) to obtain aerosol optical properties has been well established and their proficiency has been demonstrated (Kim et al., 2008; Kim et al., 2016; Lim et al., 2018, Zhang et al., 2020). However, the visible to

infrared (VIS–IR) wavelength channels that are usually employed by meteorological satellite sensors are insufficient for the retrieval of aerosol height information from observed radiances. Geostationary hyperspectral spectroscopy employed by the Geostationary Environment Monitoring Spectrometer (GEMS), Tropospheric Emissions: Monitoring of Pollution (TEMPO), and Sentinel-4 is expected to offer new possibilities for diurnal monitoring of aerosol height (Zoogman et al., 2011; Ingmann et al., 2012; Kim et al., 2020). The optimal estimation-based algorithm for aerosol height retrieval using the GEMS on-board GeoKompsat-2B (GK-2B) was developed using proxy data from the Ozone Monitoring Instrument (OMI) and is to be applied to operational GEMS observations (Kim et al., 2018).

In this study, we explore a geometrical method using VIS observations from two geostationary meteorological satellites to retrieve aerosol top height (ATH). Cloud top heights have been successfully retrieved using geometrical fusion of two geostationary satellite images (Lee at al., 2020), suggesting the applicability of such a method to any structures in the atmosphere. However, aerosol layers are not as optically thick as clouds and their heights are much lower than cloud tops, so the applicability and accuracy of the geometrical method for estimating ATH remain unresolved. Our aims were to investigate the sensitivity of ATH to observed parallax, and to validate our results by comparison with other aerosol profile datasets. The datasets used are described in Section 2. Section 3 introduces a stereoscopic ATH retrieval algorithm, and Section 4 assesses the sensitivity and uncertainty of the height retrieval algorithm based on pairs of sensors. Section 5 discusses the ATH results and compares them with spaceborne and ground-based lidar data. Finally, Section 6 summarizes the skill of the algorithm and suggests prospects for future studies.

2 Data

2.1 Satellite observation data

2.1.1 Advanced Himawari Imager

The AHI is a meteorological instrument on-board the Japanese satellites Himawari-8 and -9, which were launched on 7 October 2014 and 2 November 2016, respectively. The AHI continues the mission of the Multi-Functional Transport Satellite (MTSAT) with enhanced specifications of 16 spectral bands, including 3 VIS, 1 near-IR (NIR), 2 shortwave IR, and 10 IR channels. Two of the VIS bands have spatial resolutions at the sub-satellite point of 1 km (blue, green; 0.47, 0.51 μm), and the other is at 0.5 km resolution (red; 0.64 μm). Full-disk AHI scans are conducted every 10 min. The Image Navigation and Registration (INR) variation for AHI is less than 0.5 pixels for VIS bands, or ~500 m for the 1 km resolution bands (blue, red) and 250 m for the 500 m resolution band (green) (Tabata et al., 2016).

The AHI AOD data from the Yonsei AErosol Retrieval (YAER) algorithm are used as a criterion for the selection of retrieval pixels. The YAER algorithm is a multi-channel algorithm based on three VIS and one NIR AHI channels. The product demonstrates good agreement with Aerosol Robotic Network (AERONET) AOD data (Lim et al., 2018). It should

be noted here that AOD is simply a criterion for retrieval pixel selection, and uncertainties in AOD are not relevant to the accuracy of the stereoscopic ATH algorithm.

2.1.2 Advanced Meteorological Imager

The Advanced Meteorological Imager is a GEO meteorological instrument on-board Geo-Kompsat 2A (GK-2A), which was launched on 4 December 2018 by the National Meteorological Satellite Center (NMSC) of Korea and has more channels of higher spatial resolution and succeeds the mission of its MI predecessor. The AMI spectral bands are similar to those of AHI, except for a VIS and IR band; the center wavelengths and spatial resolutions of the VIS bands of AMI and AHI are similar. The AMI also carries out full-disk scans every 10 min. An AMI INR evaluation on 31 July 2019 indicated an absolute navigation error of <1.0 pixel (~1 km) for 1 km resolution bands and 0.9 pixels (~450 m) for 500 m bands. The required INR performance was 1.50 km for 1 km resolution bands, and 0.75 km for 500 m resolution bands (Kim et al., 2021). The NMSC reports the navigation performance of GK-2A on a regular basis (https://nmsc.kma.go.kr/homepage/html/satellite/quality/selectQualityGk2a.do), with monthly navigation performance reports from 2020 indicating average navigation errors of 9–13 and 8–18 µrad for the latitudinal (N–S) and longitudinal (E–W) directions, respectively. Aside from a few cases of extreme INR error, navigation errors in either direction have typically fluctuated by <20 µrad since May 2020, whereas those of the N–S direction before April 2020 frequently exceeded 20 µrad (although they were usually <40 µrad).

2.1.3 Advanced Geostationary Radiation Imager

The Chinese geostationary satellite Feng-Yun-4A (FY-4A), which was launched on 11 December 2016, carries the Advanced Geostationary Radiation Imager (AGRI), the Geostationary Interferometric Infrared Sounder (GIIRS), and the Lightning Mapping Imager (LMI). The AGRI observes 14 VIS–IR spectral bands, but with only two VIS bands of blue and red (0.47 and 0.68 µm) that have spatial resolutions of 1 and 0.5 km, respectively. AGRI performs 40 full-disk scans per day, using observations from every hour to match the times to the other sensors. The INR requirement for AGRI is 112 µrad or ~4 km on the surface (Yang et al., 2017).

2.2 Data intercomparison

Their ability of lidar observations to produce aerosol profile data with high vertical resolution enables them to be a validation standard for spaceborne aerosol height retrieval algorithms. Spaceborne lidars such as CALIOP enable validation of aerosol height over broad spatial ranges and areas where ground-based lidars are unavailable. Several studies have thus used CALIOP data to validate their algorithms (Lee et al., 2015; Nanda et al., 2020; Chen et al., 2021; Lee et al., 2021). Despite their shortcoming in terms of sparse observational coverage, ground-based lidars facilitate the validation of diurnal variations

in aerosol height. In this study, we used both spaceborne and ground-based lidar data for comparisons among stereoscopic ATH algorithm products.

2.2.1 CALIOP

125 The Cloud–Aerosol Lidar and Infrared Pathfinder Satellite Observations (CALIPSO) satellite was launched on 28 April 2006 on a sun-synchronous orbit, and it revisits the same ground track every 16 days. CALIOP, the primary instrument on-board CALIPSO, is a two-wavelength polarization lidar optimized for global profiling of cloud and aerosol distributions. CALIOP measures the returning signals of pulses at 532 and 1064 nm that are produced simultaneously by the laser. Two receivers of the 532 nm channel, both of which can detect polarization signals, measure the degree of linear polarization of

130 the returning signal. Using the signals of the two 532 nm channels and a total 1064 nm returning signal, CALIOP obtains accurate information on cloud and aerosol height (Winker et al., 2007). The standard output aerosol profile product includes total, parallel, and perpendicular backscatter at 532 nm, extinction coefficients (ECs), particulate depolarization ratios at 532 nm, and volume backscatter and ECs derived from the 1064 nm channel. Data are reported at a uniform spatial resolution of 60 m (vertical) and 5 km (horizontal). Vertical resolutions are coarser at higher altitudes because of CALIPSO's onboard

135 data-averaging scheme. For the sake of data quality, we used aerosol extinction data satisfying cloud–aerosol discrimination (CAD) scores of −20 to −100 (with CAD scores closer to −100 having high confidence) and extinction quality control flags of 1 and 2 at 532 nm.

2.2.2 Korean Aerosol Lidar Observation Network

Aerosol extinction profile data from ground-based lidars provide quantitative information on aerosol vertical distributions.
140 Without surface interference, an aerosol extinction profile can be obtained from the returning signal of a ground-based lidar using the lidar equation (Welton et al., 2000). The lidar ratio, which depends on aerosol type, must be assumed from previous studies or sun-photometer observations near the lidar site. Attenuation of a thick aerosol layer by low-level cloud decreases the signal-to-noise ratio, preventing aerosol extinction profile retrieval. The Korean Aerosol LIDAR Observation Network (KALION) is a network of aerosol lidars providing real-time monitoring of aerosol formation and transport over

145 Korea. Lidar observation images at each site in Korea are updated daily on the KALION website (http://www.kalion.kr). Six lidar sites operated by five institutes on the Korean Peninsula undertake continuous observations of aerosol formation and transport. Here, we used total attenuated backscatter data from lidar sites in Seoul (SNU) and Gosan (GSN), maintained by Seoul National University (Yeo et al., 2016), for comparison with results from the stereoscopic ATH algorithm. KALION total attenuated backscatter profiles have a vertical resolution of 60 m and temporal resolution of 15 min.

3 Stereoscopic ATH algorithm

3.1 Overview

The stereoscopic ATH algorithm is developed based on the concept of cloudtop height retrieval (Fig. 1; Nelson et al., 2013; Lee et al., 2020). It begins with a resampling procedure, bringing one geolocation coordinate to the other. The AHI geolocation is set as a reference to fix the top-of-atmosphere (TOA) reflectance images of the AMI and AGRI. The TOA reflectance in any channel within the VIS–NIR range is available because aerosols are optically apparent in VIS–NIR-band observations. However, the land surface is brightest at longer wavelengths and the ocean surface is brightest at shorter wavelengths (von Hoyningen-Huene et al., 2010). Short VIS bands such as blue (470 nm) and green (510 nm) thus suffer interference from ocean surface signals, and the NIR band (850 nm) from land surface signals. To avoid errors induced by the surface signal, we used red band (640 nm) TOA reflectance.

After resampling, the parallax was calculated during the image-matching process, with parallax being defined as the effect by which the position of an object appears to change when the object is seen from different positions, such that when an aerosol layer is seen at different GEO orbits, it appears to be above different points on Earth. The higher the aerosol layer is, the longer the parallax is. Therefore, by identifying identical aerosol layers from each satellite images, parallax can be calculated by measuring the distance between the two points on Earth over which the aerosol layer appears to be located. Finally, a simple 3-dimensional (3D) parallax height conversion equation was defined to determine the height of the aerosol layer.

Different algorithms have employed individual definitions of aerosol height (Sun et al., 2019). Here, the retrieval product is defined as ATH measured from the surface of a spherical Earth of radius of 6378.2 km. In our stereoscopic ATH retrieval algorithm, parallax is formed by the highest feature that is optically thick enough to screen signals below. Regardless of the thickness of the bottom of the aerosol layer, the algorithm returns the altitude of the top of the layer that is optically thick at VIS wavelengths. For multiple-layer aerosols, if the thick upper layer blocks radiance from the lower layer, the algorithm is intended to return the top height of the upper layer. However, an elevated upper layer aerosol of moderate thickness can complicate the image-matching process and may induce retrieval error. In Fig. 2, scanning points on the ground (A' and B') from satellites A and B are projected on the sphere above. As the distance between two scanning points (parallax) is calculated assuming the same spherical Earth, the ATH converted from the parallax is the altitude from the surface of the sphere. To summarize, the final product of aerosol height in this study is defined as the ATH from a spherical Earth.

3.2 Resampling

For a stereoscopic ATH algorithm, two different instruments at different locations act as the two eyes of a human observer. Their different perspectives make one image from a satellite distorted relative to the other. In that case, it is difficult for computers to recognize that the two satellites are seeing the same object. Therefore, the geolocation of one satellite must be fixed relative to the other. Here, the image to be resampled is referred to as "A", and that of the reference geolocation as "B".

Resampling makes use of a k-dimensional tree method to find the nearest points of A from the geolocation of B. The k-dimensional tree is a fast algorithm locating the nearest neighbors of a point (B) to a k-dimensional tree of points (A) (Maneewongvatana and Mount, 1999). After converting two images from the geographic (spherical) coordinate system to a

185   Cartesian coordinate system, a k-dimensional tree based on image A is used to find the 10 nearest neighbors of image B. The resampled image of A is a simple average of the 10 nearest points of A within 5 km of point B.

3.3 Parallax estimation

Parallax is calculated using a moving window correlation technique. The method finds matching aerosol features in two images by finding the best-correlated TOA reflectance image windows from each satellite, assuming that an aerosol feature

190   is optically thick enough to be distinguishable from the background surface. The window is therefore set around a pixel of AOD > 0.6 (the absolute values of AOD are of no consequence to the retrieved ATH values). We set a fixed window of 33 × 33 pixels from image B, and the correlation coefficients of the fixed window in image A with moving windows of the same size are calculated. The moving window moves from −7 pixels to +7 pixels in the latitudinal and longitudinal directions, starting from the same longitude/latitude as the fixed reference window. Finally, the parallax of a lofted aerosol layer is

195   defined as the distance between the centers of the fixed and moving windows with the greatest correlation coefficient among 225 moving windows. If the highest correlation coefficient does not exceed 0.9, the pixel is excluded from the retrieval.

Window size may influence the correlation between the two windows. A window size too small would not be optimal in deciding whether the images are the same; with too large a window, radiance from an adjacent cloud or a distinct land feature causes respectively higher or lower correlation coefficients. The moving range of the moving windows dictates the

200   maximum retrieved aerosol height. The moving range of ±7 pixels in both the latitudinal and longitudinal directions means that maximum parallax would be the distance equivalent to $7\sqrt{2}$ pixels. In this study, the size and moving range of the windows were decided empirically.

Because the method calculates distances between each grid point, the calculated values of parallax are discrete. The distance of the center of a window from that of the nearest window is ~1 km, and the next nearest is at ~1.414 ($\sqrt{2}$) km near the

205   satellite nadir point. The closest value of parallax is thus discrete at ~0.4 km difference. This discrete parallax is converted to height by a parallax–height conversion relationship. Gaps in parallax values are larger with increasing distance from the nadir point, so retrieved heights are not necessarily spatially continuous.

3.4 Parallax–height conversion

A graphical description of the parallax–height conversion process is given in Fig. 2. GEO orbits are always above the

210   Equator, so the 2D conversion method used with LEO orbit satellites (e.g., MINX algorithm) had to be adjusted to a 3D scheme. Assuming an aerosol layer at point P, for a layer of height of h above a ground point P', the parallax is the distance between the ground scanning points of satellites A and B (A' and B'). Based on the longitude and latitude of A' and B', the

zenith and azimuth angles at each point are calculated. The determination of aerosol height can then be summarized as follows:

215 $(\overline{A'P'}) = h \tan\alpha$, $(\overline{B'P'}) = h \tan\beta$, (1)

$\angle A'P'B' = \gamma - \theta$. (2)

From the cosine law:

$d^2 = h^2(\tan^2\alpha + \tan^2\beta) - 2h^2 \tan\alpha \tan\beta \cos(\gamma - \theta)$, (3)

and

220 $h = \dfrac{d}{\sqrt{\tan^2\alpha + \tan^2\beta - 2\tan\alpha \tan\beta \cos(\gamma - \theta)}}$, (4)

where h is ATH, d is the parallax, α and β are the viewing zenith angles of A and B, and γ and θ are the viewing azimuth angles of A and B. Geometrical values $(\alpha, \beta, \gamma,$ and $\theta)$ are determined by the locations of satellites A and B and the ground position of the aerosol layer. Based on the estimated parallax (sections 3.2 and 3.3), the layer height of the aerosol is then retrieved.

225 Although highly reflective clouds can interfere with correlation calculations, the stereoscopic ATH algorithm does not include a cloud masking procedure. By using the AHI AOD product, where retrievals are undertaken only for cloud-free pixels, we assume that selected pixels with high AOD are cloud free. However, a moving window for aerosol height retrieval may include some cloud pixels, resulting in overestimation of aerosol heights. Therefore, retrieval values of >10 km are removed after the retrieval process.

230 **4 Sensitivity and uncertainty analyses**

Retrieval sensitivity and uncertainty assessments involved methods that differ from traditional methods involving radiative transfer models simulating observations. For example, a sensitivity study of aerosol layer height (not ATH) retrieval from the O$_2$ A band (Hollstein and Fischer, 2014) included spectral resolution, instrumental noise, and surface inhomogeneity, whereas the sensitivity of the stereoscopic ATH retrieval algorithm was based on the proficiency of parallax calculations,

235 which are a function of aerosol height and the distance between two satellites. Moreover, parallax calculations only use the spatial patterns of observed radiances from satellite images. This implies an advantage in using the parallax of two satellite images, in that the geometrical method does not suffer from sensor calibration problems, with the unstable radiometric performance of AGRI (Zhong et al., 2021) being unlikely to affect the results.

Unlike traditional algorithms that simulate satellite measurements in assessing the sensitivity and uncertainty of radiative

240 transfer models, quantitative stereoscopic ATH retrieval assessments involve a simple geometrical estimation of parallax. Furthermore, rather than other complex possible causes of retrieval uncertainty, such as signals from bright surfaces and

radiation path lengths, a simple cause of retrieval uncertainty was involved here: the INR error. Intrusion of the INR error during the retrieval process falsely locates level 1B images and affects parallax calculations, which are directly related to an error in ATH retrieval.

4.1 Sensitivity

Parallax is greater when the aerosol layer is at a high altitude or when the two satellites are farther apart (Fig. 2). The theoretical parallax variation with aerosol height and satellite location can be calculated for quantitative assessment of retrieval sensitivity using Eq. (3). Based on the viewing geometry of Seoul, South Korea (37° N, 127° E), and setting one satellite imager as the AHI (140.7° E), the calculated parallax according to the location of the other satellite and the altitude of the aerosol layer is as shown in Fig. 3. Using two satellite images with 1 km spatial resolution, parallax distances of <1 km cannot be resolved (Section 3.2). Considering that the image resolution coarsens with increasing distance from the sub-satellite point, the possible minimum parallax that can be resolved from two satellite images will be >>1 km. It follows that a pair of 1 km image-resolution satellite imagers are unable to retrieve aerosol heights that demand resolution of a parallax of <1 km. As the location of the other satellite imager approaches AHI, the parallax decreases rapidly (Fig. 3). This implies that a set of satellites too close to each other involves less parallax, which is a challenging condition for geometrical height retrieval. For example, an aerosol layer with a height of 2 km produces ~2 km of parallax using an AHI–AGRI pair at 104.7° E, which is sufficient for 1 km resolution. However, an AHI–AMI pair at 128.2° E cannot resolve this aerosol layer, as the parallax is ~0.75 km. To retrieve a lower aerosol height, satellites must be farther apart. When an aerosol layer is at lower altitudes, the parallax gradient is greater when the two satellites are closer, which means that the closer the pair of satellites, the greater possibility of small uncertainties during parallax calculations may produce larger errors in retrieval height. The parallax gradient becomes linear as the aerosol layer height increases. Two satellite imagers with insufficient separation are thus unfavorable for geometrical height retrieval. However, as the satellites get farther apart, the spatial resolution becomes coarser within their overlapping area. This implies that the possible minimum parallax may be greater than expected, and the minimum height that a pair of satellites can resolve would be greater in the off-nadir region.

Viewing geometries (α, β, γ, and θ; Fig. 2) are also functions of location on Earth. A contour of theoretical minimum height that two pairs of satellites (AHI–AGRI and AHI–AMI) can resolve using 1 km spatial-resolution bands is shown in Fig. 4. The theoretical minimum retrievable height decreases with distance from the center point of the two satellites. In terms of latitude, viewing zenith angles (α and β of Eq. (4)) increase with distance from the Equator. For longitude, the difference in viewing azimuth angles ($\gamma - \theta$ in Eq. (4)) is lowest at the central longitude of the two satellites. For the AHI and AGRI (Fig. 4a), the minimum height differs by a few hundred meters in East Asia, so the location on Earth would have little impact on the results. However, the AHI and AMI are too close together to retrieve aerosol heights of <3 km over the Yellow Sea. Furthermore, the minimum retrievable height gradient along location is larger for the AHI–AMI pair, which means that retrieval error caused by parallax uncertainty is more complex for this pair of satellites. Therefore, the AHI–AGRI are better

able to retrieve aerosol heights over East Asia. Results for the two satellite pairs (AHI–AMI and AHI–AGRI) are further
275   compared in Section 5.

4.2 Uncertainty analysis

ATH retrieval uncertainties induced by 1 km latitudinal and longitudinal INR shifts are shown in Fig. 5. Uncertainty is
defined as the difference between original ATH and height calculated using parallax considering 1 km shifts in AHI
geolocation. The magnitude of uncertainty is larger when INR error is present in the longitudinal direction. When retrieving
280   ATH for an aerosol layer reaching up to 5 km altitude, the possible retrieval error caused by 1 km longitudinal INR error is
~80 m, or about four times the maximum retrieval error for 1 km latitudinal INR error. The effects of latitudinal and
longitudinal INR error on ATH retrieval uncertainty are thus quite different. In the latitudinal direction, the retrieval height
uncertainty increases with the distance between the two satellites, whereas longitudinal INR error causes equal retrieval
uncertainty regardless of the separation of the two satellites. This difference arises from the use of geostationary satellites. A
285   longitudinal INR shift can simply be regarded as one satellite moving toward or away from the other along the Equator.
Although the height retrieval algorithm is more robust with regard to parallax calculation errors when the two satellites are
far apart (Section 4.1), the retrieval error itself increases with the distance between the two satellites when latitudinal INR
errors are present. However, considering the actual INR errors of the satellites (approximately 0.5, 1, and 4 km at channels
with 1 km resolution for AHI, AMI, and AGRI, respectively), the INR error would not be of concern for the retrieval of
290   aerosol heights of a few kilometers.

5 Results and Discussion

5.1 Comparison with CALIOP aerosol profile

For qualitative comparison of retrieved ATH with CALIOP, a concise definition of CALIOP ATH (hereafter, CALIOP
height) is required for the individual algorithm. Definitions of aerosol height using the same lidar data can differ according to
295   how each algorithm defines its aerosol height products. For example, Lee et al. (2015) developed Aerosol Single-scattering
albedo and layer Height Estimation (ASHE) algorithm and compared their retrieval results with ATH based on CALIOP
aerosol total backscattering coefficient (TBC) profile, with ATH being the altitude with a TBC of 0.03 km^{-1} sr^{-1} from the top
of the profile. Lee et al. (2021) then developed a new, near production-ready ASHE algorithm, that no more retrieves ATH
because of detail differences from original ASHE algorithm. So, they had to compare the results with newly defined
300   CALIOP height, which is an aerosol extinction-weighted mean height. Considering that the concept of the stereoscopic
algorithm in this study is supposed to retrieve ATH, we generated CALIOP height in a manner similar that of Lee et al.
(2015). The total EC in the 532 nm channel (EC532) was used because the ATH product was also processed using VIS-

channel observations of satellite instruments. We therefore define CALIOP height as the height where the cumulative EC532 represents 90 % of the total column integrated EC532, starting from the bottom of the profile.

5.1.1 Case studies

Figure 6 shows a comparison of stereoscopic ATH products from the two pairs of geostationary imagers, alongside a CALIOP aerosol extinction profile for 23 January 2020 as CALIOP passed over the western Yellow Sea. The AHI AOD was valid over Beijing, Shandong Peninsula, and the ocean between the Beijing and Shandong peninsulas. The stereoscopic ATH retrieval was valid mainly over the ocean, with AOD > 0.6. Results for the two different pairs of geostationary imagers (AHI–AGRI and AHI–AMI) are shown in Fig. 6c and d. The ATH retrieved from the AHI–AGRI pair was ~2 km, and that from AHI–AMI was ~4 km. ATH retrieval along the CALIOP path is shown with CALIOP EC and height in Fig. 6e. To collocate the ATH product with CALIOP geolocation, stereoscopic ATHs within 5 km of CALIOP ground pixels were averaged. The ATH from the AHI–AGRI pair agreed well with the CALIOP height of 1–2 km on collocated pixels. The ATH retrieved from the AHI–AMI pair near 37.5° N seems to have similar values to CALIOP (or the ATH of AHI–AGRI). The scatterplot (Fig. 6f) shows CALIOP height versus stereoscopic ATH. The percent within expected error (EE%) (1 km) represents the fraction of stereoscopic ATH within 1 km of CALIOP height in total collocated pixels. In this case, all valid AHI–AGRI ATH retrievals were within 1 km of CALIOP height, whereas for AHI–AMI ATH, only 18.5 % of the total collocated ATHs were within 1 km of CALIOP height, and 33.3 % were within 1.5 km. Furthermore, several AHI–AMI ATH points have values of zero because of a lack of sensitivity to parallax induced by aerosol layers at <2 km height. Considering that the collocation of stereoscopic ATH and CALIOP height involved the averaging of ATH values, values out of retrieval sensitivity (<3 km) are may be products of averaging values of 0 km and 4 km near the CALIOP path.

The case of 8 April 2020 is shown in Fig. 7. A thick aerosol layer with AOD > 1.0 (reaching near 2.0 at the thickest part of the layer) was under a cloudy sky in Jinan, China, with low-level thin clouds along 32° N latitude. Unlike clouds over the northern part of the area, ATH overestimation by these thin clouds does not appear high enough to be screened out during the quality control procedure for the AHI–AGRI pair. Results (Fig. 7c) indicate that the retrieved ATH over the area spans from 2 to 5 km, excluding overestimation of ~10 km caused by the thin clouds. The ATH results for the AHI–AMI pair (Fig. 7d) are similar. Retrieved values of >10 km were omitted during the quality control procedure, so cloud contamination is not reflected in the result. The actual profile of aerosol ECs observed by CALIOP (Fig. 7e) suggest that the retrieved ATH for both pairs spanning from 2 to 5 km appears reasonable. Results for the AHI–AGRI pair agree more with CALIOP height at most collocated points. The EE% values for 1 km within CALIOP height for AHI–AGRI and AHI–AMI are 72.5 % and 61.3 %, respectively (Fig. 7f); those for 1.5 km are 55.0 % and 32.5 %, respectively.

The sensitivity test results (Section 4) are consistent with actual retrieval cases. From these two cases of comparison between ATH retrieval comparison and CALIOP, the performance of the stereoscopic ATH algorithm for an aerosol layer at lower or higher altitudes in the troposphere can be assessed. When an aerosol layer is under 3 km (as on 23 January 2020), the

335   stereoscopic ATH algorithm with the pair of closer satellites (AHI–AMI) failed to retrieve aerosol height. However, if the satellite separation has sufficient sensitivity for the retrieval of aerosol heights of <3 km, the geometrical height retrieval algorithm for atmospheric structure is applicable. Another case of lower aerosol layer retrieval (Fig. S1) shows the same result as that of 23 January 2020. In contrast, when an aerosol layer is at an altitude of >3 km, retrieval using a pair of closer-spaced satellites becomes possible, although retrieval accuracy increases with satellite separation. The AHI–AGRI ATH EE%

340   on 8 April 2020 was significantly lower than that on 23 January, possibly because the aerosol layer was thinner. Unlike the first case, the CALIOP EC profile of the latter case has few values of >0.3 cm^{-1}, meaning that the AHI AOD may have been overestimated. However, the possibility of systematic worsening of the retrieval accuracy of lofted aerosols remains because complex vertical features (e.g., multi-layer aerosols) make aerosol height retrieval challenging. Further data analysis is required to determine whether the deterioration in accuracy with higher ATH is systematic.

345   **5.1.2 Long-term comparison with CALIOP height**

Scatterplots of CALIOP height versus stereoscopic ATH for the study period (Fig. 8) indicate the overall performance of the stereoscopic ATH retrieval algorithm. Collocation was undertaken in the same manner as conducted in the case studies. As expected, the general retrieval performance using the AHI–AGRI pair was better than with the AHI–AMI pair. The fraction of scene-averaged ATH within 2 km of CALIOP height was 71.3 % for AHI–AGRI and 49.3 % for AHI–AMI (46.2 % and

350   21.3 %, respectively, for 1 km). For the study period, most cases had an average height of <3 km (depending on location), which was beyond the sensitivity range of the AHI–AMI pair. The stereoscopic AHI–AMI ATH (Fig. 8b) had no values of <3 km. The ATHs of the aerosol layer below the height of retrieval sensitivity were clustered around 4 km, with some at around 8 km. This difference in retrieval error may be due to horizontal homogeneity of the aerosol layer. If an aerosol layer has a spatially widespread and smooth pattern, the image matching process in the algorithm finds the nearest moving

355   window that has sufficient parallax for retrieval sensitivity. This type of error is shown by retrieval heights of 3–4 km over the Yellow Sea. Conversely, when an aerosol layer has a complex spatial pattern, the image matching is unstable, with parallax being calculated using a moving window far from where it should be. This results in much larger values of ATH than with for earlier cause of overestimation, with the maximum values of correlation being moderate.

Frequency distributions of the difference of stereoscopic ATH and CALIOP height are shown in Fig. 9. For the period from

360   January 2020 to April 2021, 2070 pixels over 143 days were collocated for the AHI–AGRI pair, and 2516 pixels over 150 days for the AHI–AMI pair. The peak of the difference between AHI–AGRI ATH and CALIOP height was near zero (Fig. 9a), with an average difference of +0.14 km, (standard deviation 2.46 km). The AHI–AMI ATH displayed peaks at −4, 2, and 6 km, with an average difference of +1.8 km (standard deviation 2.51 km). The highest peak at 2 km was due mainly to overestimation of the lower aerosol layer. The increase in frequency at specific values was due to parallax estimation giving

365   discrete values through image resolution (Section 3.2). Although ATH values were spatially averaged, discontinuous spatial features may still occur. The difference between land and ocean results appears to be negligible for both pairs of satellites,

suggesting that the surface signal that may cause uncertainty over land is negligible for a geometrical aerosol height retrieval algorithm using red band.

5.2 Comparison with ground-based lidar

370 Examples of the stereoscopic ATH algorithm capturing hourly variations of aerosol vertical features are shown in Fig. 10. Comparisons with ground-based lidar data were undertaken using only the AHI–AGRI results, which proved to be most accurate. For the spatial collocation, valid retrievals within 5 km of ground-based lidar sites were averaged. For 7 April 2020 (Fig. 10a and b), ATH was compared with observations at the SNU station. The hourly ATH map (Fig. 10a) indicates the initiation of transport of an aerosol layer with an ATH of >7 km. Upon reaching the Korean Peninsula, the aerosol layer

375 descended and dissipated. According to aerosol extinction data from ground-based lidar, the aerosol layer became thinner both geometrically and optically. The hourly variation of retrieved height began from 2.3 km at 01:00 UTC, reaching 1.7 km at 07:00 UTC. The retrieved ATH plunged to 1.1 km at 02:00 UTC, and the stereoscopic ATH retrieval algorithm captured its descent. The ATH maps (Fig. 10a) seem continuous, so the inconsistent value at 02:00 UTC may have been caused by a sampling problem, although the INR error of AMI during the early days of observations may also have been a factor.

380 Launched in late 2019, the AMI INR seemed unstable before May 2020, according to NMSC INR reports. In some cases, the latitudinal INR error increased to a few hundred (even thousands) of μrad. Another possibility is the error caused by the difference of observation time between the two sensors. The AHI performs a full-disk scan in 10 minutes, whereas the AGRI takes 15 min, starting at the top of the hour. Therefore, when strong horizontal air motion is present, a small difference in observation time between two imagers may have a significant impact on parallax calculations during stereoscopic ATH

385 retrieval. Aerosol long-range transport involves strong westerlies in East Asia, so the observation time difference may also be the source of retrieval error. Lee et al. (2018) addressed this problem by interpolating observation times from one satellite to match the other. Considering that the percentage of stereoscopic ATH within 1 km from CALIOP height was 46.2 %, the fluctuation at 02:00 UTC may simply be regarded as the expected retrieval error. On 9 April 2020 (Fig. 10c and d), ATH was compared with aerosol extinction at Gosan station (GSN). In that case, ground-based lidar data showed the top of the

390 stable aerosol layer to be ~2 km. Stereoscopic ATH also indicated an altitude of 2 km with a slight increase at 06:00 UTC, following the same increase of ground-based lidar data. Use of geostationary satellites enables the analysis of diurnal variations in ATH. The former case indicates how the vertical structure of an aerosol layer changes during long-range transport, whereas the latter represents a case of a thin but stable aerosol layer.

6 Conclusions

395 A stereoscopic ATH retrieval algorithm was developed on the basis of a geometrical height calculation method applying to any structure in the atmosphere. The advantages of such a method are that sensor calibration does not affect results and expensive radiative transfer computations are not required. Furthermore, the method is not affected by variations in aerosol

optical properties. As a result of a sensitivity study, a well-separated satellite pair was found to be a better choice for stereoscopic ATH retrieval. Coarser spatial resolution in off-nadir areas can cause reductions in retrieval sensitivity.

400 Retrieval uncertainty due to longitudinal INR shifts is greater when the two satellites are farther apart, whereas retrieval uncertainty due to latitudinal INR shift is a function of aerosol height alone. An INR performance shift of 1 km introduces a retrieval error of a few dozen of meters, which is negligible when retrieving ATH of a few kilometers. Two case studies showed that the retrieval results of an AHI–AGRI satellite pair were consistent with the CALIOP EC profile. The general performance of the stereoscopic ATH retrieval was also better with the AHI–AGRI pair, with EE% values of 71.3 % and

405 46.2 % for 2 and 1 km, respectively. For the AHI–AMI pair, EE% values were 49.3 % and 21.3 % for 2 and 1 km, respectively. The mean bias in ATH from the AHI–AGRI pair was +0.14 km, whereas the AHI–AMI pair showed a strong positive bias of +1.75 km on average, with a peak at +2 km due to a lack of sensitivity at lower aerosol layers. Comparison with ground-based lidar revealed an ability to monitor diurnal variations in aerosol height with the synergetic use of geostationary satellites. Analysis of the sensitivity and uncertainty of the stereoscopic algorithm and its application to three

410 geostationary satellite images over East Asia confirmed the capability of ATH retrieval using geometrical parallax calculations. Future work will include additional lower-level cloud screening, consideration of the difference in pixel-level scan times between two satellites, and more complex parallax–height conversion using spherical trigonometry. We expect the use of 500 m resolution red band observations with the stereoscopic ATH retrieval algorithm to provide greater sensitivity for lower-level aerosol layers with improved accuracy.

415

Code availability. The aerosol top height product data from AHI, AMI and AGRI are available on request from the corresponding author, Jhoon Kim (jkim2@yonsei.ac.kr).

Author contribution. MK, HL, and JK designed the experiment. MK carried out the data processing. HL, SL and YC

420 provided support for data. MK wrote the manuscript, with contributions from all co-authors. JK reviewed and edited the article. JK provided support and supervision. All authors analyzed the measurement data and prepared the article.

Competing interests. The authors declare that they have no conflict of interest.

425 *Acknowledgements.* We thank all principal investigators and their staff for establishing and maintaining the KALION sites and CALIOP used in this investigation. This research was supported by Korea Institute of Marine Science & Technology Promotion(KIMST) funded by the Ministry of Oceans and Fisheries, Korea(20180456).

References

Chen, X., Wang, J., Xu, X. G., Zhou, M., Zhang, H. X., Garcia, L. C., Colarco, P. R., Janz, S. J., Yorks, J., McGill, M., Reid,
J. S., de Graaf, M., and Kondragunta, S.: First retrieval of absorbing aerosol height over dark target using TROPOMI oxygen
B band: Algorithm development and application for surface particulate matter estimates, Rem. Sens. Environ., 265, ARTN
112674, doi:10.1016/j.rse.2021.112674, 2021.

Choi, M., Sander, S. P., Spurr, R. J.D., Pongetti, T. J., van Harten, G., Drouin, B. J., Crisp, D., Eldering, A., Kalashnikova, O.
V., Jiang, J. H., Hyon, J. J., and Fu, D.: Aerosol profiling using radiometric and polarimetric spectral measurements in the
O2 near infrared bands: Estimation of information content and measurement uncertainties, Rem. Sens. Environ, 253, ARTN
112179, doi:10.1016/j.rse.2020.112179, 2021.

Chu, D. A., Szykman, J., Kittaka, C., Chin, M., Liu, H. C., Remer, L., Al-Saadi, J., and Winker, D.: Developing aerosol
height product from MODIS and synergy of MODIS and CALIPSO measurement for global application, IGARSS 2008 -
2008 IEEE Int. Geos. & Rem. Sens. Symposium, 7-11 July 2008, pp. IV - 303-IV - 306, doi:
10.1109/IGARSS.2008.4779718, 2008.

Gupta, G., Ratnam, M. V., Madhavan, B. L., Prasad, P., and Narayanamurthy, C. S.: Vertical and spatial distribution of
elevated aerosol layers obtained using long-term ground-based and space-borne lidar observations, Atmos. Environ., 246,
ARTN 118172, doi:10.1016/j.atmosenv.2020.118172, 2021.

Hollstein, A. and Fischer, J.: Retrieving aerosol height from the oxygen A band: a fast forward operator and sensitivity study
concerning spectral resolution, instrumental noise, and surface inhomogeneity, Atmos. Meas. Tech., 7, 1429–1441,
doi:10.5194/amt-7-1429-2014, 2014.

Huang, L., Jiang, J. H., Tackett, J. L., Su, H., and Fu, R.: Seasonal and diurnal variations of aerosol extinction profile and
type distribution from CALIPSO 5-year observations, J. Geophys. Res. Atmos., 118, 4572–4596, 10.1002/jgrd.50407, 2013.

Ingmann, P., Veihelmann, B., Langen, J., Lamarre, D., Stark, H., and Courreges-Lacoste, G. B.: Requirements for the GMES
Atmosphere Service and ESA's implementation concept: Sentinels-4/-5 and-5p, Rem. Sens. Environ., 120, 58–69,
doi:10.1016/j.rse.2012.01.023, 2012.

Jeong, U., Kim, J., Ahn, C., Torres, O., Liu, X., Bhartia, P. K., Spurr, R. J. D., Haffner, D., Chance, K., and Holben, B. N.:
An optimal-estimation-based aerosol retrieval algorithm using OMI near-UV observations, Atmos. Chem. Phys., 16, 177–
193, doi:10.5194/acp-16-177-2016, 2016.

Kim, D., Gu, M., Oh, T. H., Kim, E. K., and Yang, H. J.: Introduction of the Advanced Meteorological Imager of Geo-
Kompsat-2a: In-orbit tests and performance validation, Remote Sens-Basel, 13, ARTN 1303, 10.3390/rs13071303, 2021.

Kim, M., Kim, J., Torres, O., Ahn, C., Kim, W., Jeong, U., Go, S., Liu, X., Moon, K. J., and Kim, D. R.: Optimal estimation-
based algorithm to retrieve aerosol optical properties for GEMS measurements over Asia, Rem. Sens. Basel, 10, ARTN 162,
doi:10.3390/rs10020162, 2018.

Kim, M., Kim, J., Jeong, U., Kim, W., Hong, H., Holben, B., Eck, T. F., Lim, J. H., Song, C. K., Lee, S., and Chung, C. Y.: Aerosol optical properties derived from the DRAGON-NE Asia campaign, and implications for a single-channel algorithm to retrieve aerosol optical depth in spring from Meteorological Imager (MI) on-board the Communication, Ocean, and Meteorological Satellite (COMS), Atmos. Chem. Phys., 16, 1789–1808, doi:10.5194/acp-16-1789-2016, 2016.

465 Kim, M. H., Omar, A. H., Tackett, J. L., Vaughan, M. A., Winker, D. M., Trepte, C. R., Hu, Y. X., Liu, Z. Y., Poole, L. R., Pitts, M. C., Kar, J., and Magill, B. E.: The CALIPSO version 4 automated aerosol classification and lidar ratio selection algorithm, Atmos. Meas. Tech., 11, 6107–6135, doi:10.5194/amt-11-6107-2018, 2018.

Kim, J., Jeong, U., Ahn, M. H., Kim, J. H., Park, R. J., Lee, H., Song, C. H., Choi, Y. S., Lee, K. H., Yoo, J. M., Jeong, M. J., Park, S. K., Lee, K. M., Song, C. K., Kim, S. W., Kim, Y. J., Kim, S. W., Kim, M., Go, S., Liu, X., Chance, K., Chan Miller,

470 C., Al-Saadi, J., Veihelmann, B., Bhartia, P. K., Torres, O., Abad, G. G., Haffner, D. P., Ko, D. H., Lee, S. H., Woo, J. H., Chong, H., Park, S. S., Nicks, D., Choi, W. J., Moon, K. J., Cho, A., Yoon, J., Kim, S. K., Hong, H., Lee, K., Lee, H., Lee, S., Choi, M., Veefkind, P., Levelt, P. F., Edwards, D. P., Kang, M., Eo, M., Bak, J., Baek, K., Kwon, H. A., Yang, J., Park, J., Han, K. M., Kim, B. R., Shin, H. W., Choi, H., Lee, E., Chong, J., Cha, Y., Koo, J. H., Irie, H., Hayashida, S., Kasai, Y., Kanaya, Y., Liu, C., Lin, J., Crawford, J. H., Carmichael, G. R., Newchurch, M. J., Lefer, B. L., Herman, J. R., Swap, R. J.,

475 Lau, A. K. H., Kurosu, T. P., Jaross, G., Ahlers, B., Dobber, M., McElroy, C. T., and Choi, Y.: New era of air quality monitoring from space: Geostationary Environment Monitoring Spectrometer (GEMS), Bull. Am. Meteorol. Soc., 101, E1–E22, doi:10.1175/Bams-D-18-0013.1, 2020.

Koffi, B., Schulz, M., Breon, F. M., Griesfeller, J., Winker, D., Balkanski, Y., Bauer, S., Berntsen, T., Chin, M. A., Collins, W. D., Dentener, F., Diehl, T., Easter, R., Ghan, S., Ginoux, P., Gong, S. L., Horowitz, L. W., Iversen, T., Kirkevag, A.,

480 Koch, D., Krol, M., Myhre, G., Stier, P., and Takemura, T.: Application of the CALIOP layer product to evaluate the vertical distribution of aerosols estimated by global models: AeroCom phase I results, J. Geophys. Res. Atmos., 117, ARTN D10201, doi:10.1029/2011jd016858, 2012.

Lee, J. H., Hsu, N. C., Sayer, A. M., Seftor, C. J., and Kim, W. V.: Aerosol layer height with enhanced spectral coverage achieved by synergy between VIIRS and OMPS-NM measurements, IEEE Geosci. Rem. Sens., 18, 949–953,

485 doi:10.1109/Lgrs.2020.2992099, 2021.

Lee, J., Hsu, N. C., Bettenhausen, C., Sayer, A. M., Seftor, C. J., and Jeong, M. J.: Retrieving the height of smoke and dust aerosols by synergistic use of VIIRS, OMPS, and CALIOP observations, J. Geophys. Res. Atmos., 120, 8372–8388, doi:10.1002/2015jd023567, 2015.

Liao, T. T., Gui, K., Li, Y. F., Wang, X. Y., and Sun, Y.: Seasonal distribution and vertical structure of different types of

490 aerosols in southwest China observed from CALIOP, Atmos. Environ., 246, ARTN 118145, doi:10.1016/j.atmosenv.2020.118145, 2021.

Lim, H., Choi, M., Kim, J., Kasai, Y., and Chan, P. W.: AHI/Himawari-8 Yonsei Aerosol Retrieval (YAER): Algorithm, validation and merged products, Rem. Sens. Basel, 10, ARTN 699, doi:10.3390/rs10050699, 2018.

Michailidis, K., Koukouli, M. E., Siomos, N., Balis, D., Tuinder, O., Tilstra, L. G., Mona, L., Pappalardo, G., and Bortoli, D.:
First validation of GOME-2/MetOp absorbing aerosol height using EARLINET lidar observations, Atmos. Chem. Phys., 21,
3193–3213, doi:10.5194/acp-21-3193-2021, 2021.

Nanda, S., de Graaf, M., Veefkind, J. P., Sneep, M., ter Linden, M., Sun, J. Y. T., and Levelt, P. F.: A first comparison of
TROPOMI aerosol layer height (ALH) to CALIOP data, Atmos. Meas. Tech., 13, 3043–3059, doi:10.5194/amt-13-3043-
2020, 2020.

Nelson, D. L., Garay, M. J., Kahn, R. A., and Dunst, B. A.: Stereoscopic height and wind retrievals for aerosol plumes with
the MISR INteractive eXplorer (MINX), Remote. Sens. Basel, 5, 4593–4628, doi:10.3390/rs5094593, 2013.

Sun, J. Y. T., Veefkind, P., Nanda, S., van Velthoven, P., and Levelt, P.: The role of aerosol layer height in quantifying
aerosol absorption from ultraviolet satellite observations, Atmos. Meas. Tech., 12, 6319–6340, doi:10.5194/amt-12-6319-
2019, 2019.

Tabata, T., Andou, A., Bessho, K., Date, K., Dojo, R., Hosaka, K., Mori, N., Murata, H., Nakayama, R., Okuyama, A., and
Takahashi, M.: Himawari-8/AHI latest performance of navigation and calibration, Proc. SPIE, 9881, ARTN 98812j,
doi:10.1117/12.2240200, 2016.

Tian, P. F., Cao, X. J., Zhang, L., Sun, N. X., Sun, L., Logan, T., Shi, J. S., Wang, Y., Ji, Y. M., Lin, Y., Huang, Z. W., Zhou,
T., Shi, Y. Y., and Zhang, R. Y.: Aerosol vertical distribution and optical properties over China from long-term satellite and
ground-based remote sensing, Atmos. Chem. Phys., 17, 2509–2523, doi:10.5194/acp-17-2509-2017, 2017.

Vijayakumar, S., Narayan, S., Yang, C. C., Boerner, P., Jacob, R., Mathai, M., Harse, R., and Purdy, J.: Introducing new
technologies into the clinic - Benchmark dose-volume histograms for prostate cancer as a paradigm, Front. Radiat. Ther. On.,
40, 180–192, doi:10.1159/000106035, 2007.

von Hoyningen-Huene, W., Yoon, J., Vountas, M., Istomina, L. G., Rohen, G., Dinter, T., Kokhanovsky, A. A., and Burrows,
J. P.: Retrieval of spectral aerosol optical thickness over land using ocean color sensors MERIS and SeaWiFS, Atmos. Meas.
Tech., 4, 151–171, doi:10.5194/amt-4-151-2011, 2011.

Welton, E. J., Voss, K. J., Gordon, H. R., Maring, H., Smirnov, A., Holben, B., Schmid, B., Livingston, J. M., Russell, P. B.,
Durkee, P. A., Formenti, P., and Andreae, M. O.: Ground-based lidar measurements of aerosols during ACE-2: instrument
description, results, and comparisons with other ground-based and airborne measurements, Tellus B, 52, 636–651,
doi:10.1034/j.1600-0889.2000.00025.x, 2000.

Winker, D. M., Hunt, W. H., and McGill, M. J.: Initial performance assessment of CALIOP, Geophys. Res. Lett., 34, ARTN
L19803, doi:10.1029/2007gl030135, 2007.

Winker, D. M., Vaughan, M. A., Omar, A., Hu, Y. X., Powell, K. A., Liu, Z. Y., Hunt, W. H., and Young, S. A.: Overview
of the CALIPSO mission and CALIOP data processing algorithms, J. Atmos. Ocean Tech., 26, 2310–2323,
doi:10.1175/2009jtecha1281.1, 2009.

Wu, L. H., Hasekamp, O., van Diedenhoven, B., Cairns, B., Yorks, J. E., and Chowdhary, J.: Passive remote sensing of aerosol layer height using near-UV multiangle polarization measurements, Geophys. Res. Lett., 43, 8783–8790, doi:10.1002/2016gl069848, 2016.

Yang, J., Zhang, Z. Q., Wei, C. Y., Lu, F., and Guo, Q.: Introducing the New Generation of Chinese Geostationary Weather
530 Satellites, Fengyun-4., B Am. Meteorol. Soc., 98, 1637–1658, doi:10.1175/Bams-D-16-0065.1, 2017.

Yeo, H., Kim, S. W., Lee, C., Kim, D., Kim, B. G., Kim, S., Nam, H. G., Noh, Y. M., Park, S., Park, C. B., Seo, K., Choi, J. Y., Lee, M. I., and Lee, E. H.: The KALION automated aerosol type classification and mass concentration calculation algorithm, Korean J. Rem. Sens, 32, 2, 119–131, doi:10.7780/kjrs.2016.32.2.5, 2016.

Zhang, H., Kondragunta, S., Laszlo, I., and Zhou, M.: Improving GOES Advanced Baseline Imager (ABI) aerosol optical
535 depth (AOD) retrievals using an empirical bias correction algorithm, Atmos. Meas. Tech., 13, 5955–5975, doi:10.5194/amt-13-5955-2020, 2020.

Zhong, B., Ma, Y. B., Yang, A. X., and Wu, J. J.: Radiometric performance evaluation of FY-4A/AGRI based on Aqua/MODIS, Sensors-Basel, 21, ARTN 1859, doi:10.3390/s21051859, 2021.

Zoogman, P., Liu, X., Suleiman, R. M., Pennington, W. F., Flittner, D. E., Al-Saadi, J. A., Hilton, B. B., Nicks, D. K.,
540 Newchurch, M. J., Carr, J. L., Janz, S. J., Andraschko, M. R., Arola, A., Baker, B. D., Canova, B. P., Miller, C. C., Cohen, R. C., Davis, J. E., Dussault, M. E., Edwards, D. P., Fishman, J., Ghulam, A., Abad, G. G., Grutter, M., Herman, J. R., Houck, J., Jacob, D. J., Joiner, J., Kerridge, B. J., Kim, J., Krotkov, N. A., Lamsal, L., Li, C., Lindfors, A., Martin, R. V., McElroy, C. T., McLinden, C., Natraj, V., Neil, D. O., Nowlan, C. R., O'Sullivan, E. J., Palmer, P. I., Pierce, R. B., Pippin, M. R., Saiz-Lopez, A., Spurr, R. J. D., Szykman, J. J., Torres, O., Veefkind, J. P., Veihelmann, B., Wang, H., Wang, J., and Chance,
545 K.: Tropospheric emissions: Monitoring of pollution (TEMPO), J. Quant. Spectr. Ra., 186, 17–39, doi:10.1016/j.jqsrt.2016.05.008, 2017.
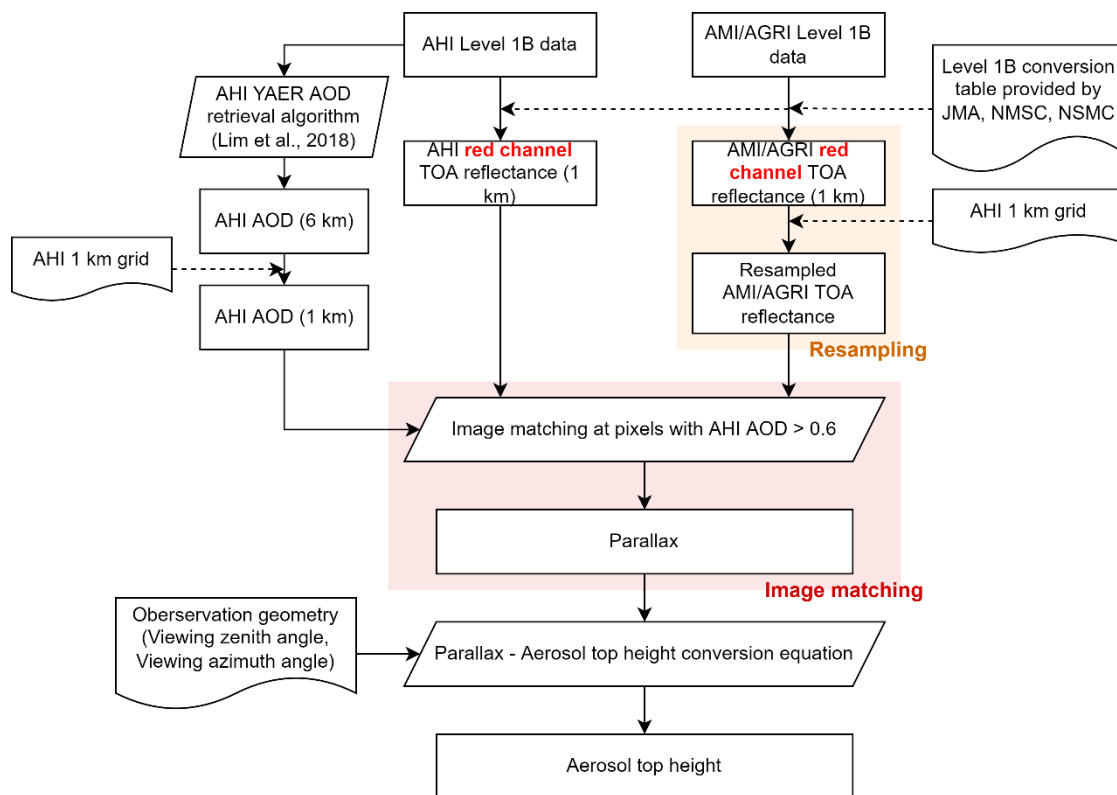
Figure 1: A flowchart of the stereoscopic aerosol top height (ATH) retrieval algorithm.

550
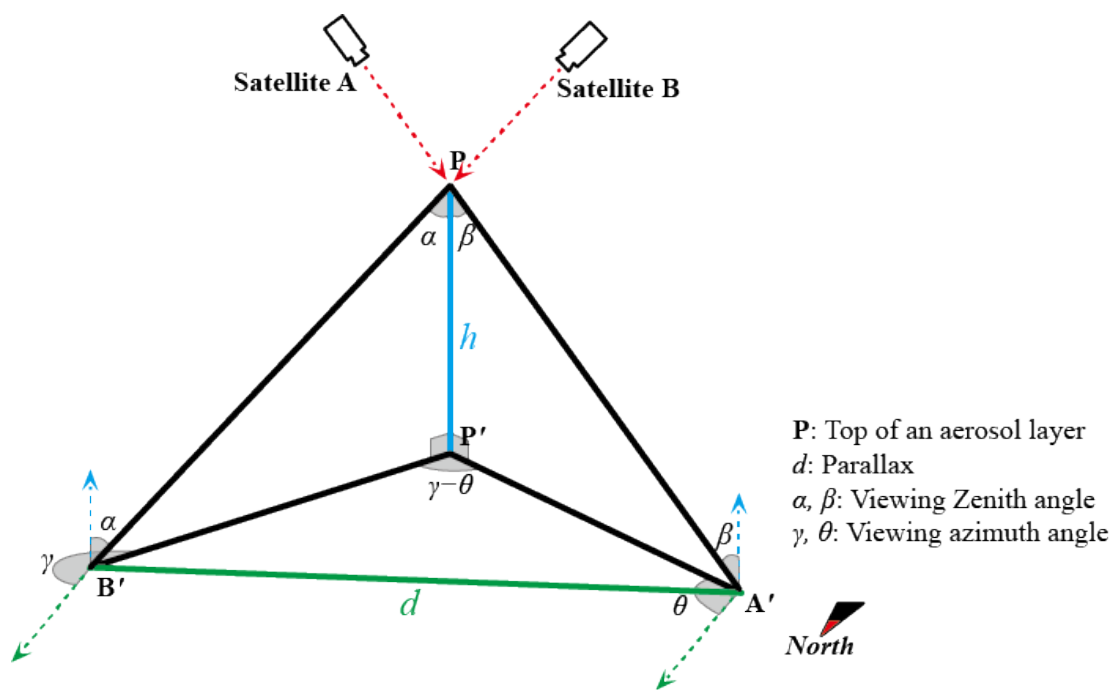
Figure 2: Graphical depiction of parallax from the top of the aerosol layer (P) observed using a pair of satellites (A and B).

Atmospheric Measurement Techniques Open Access
Discussions
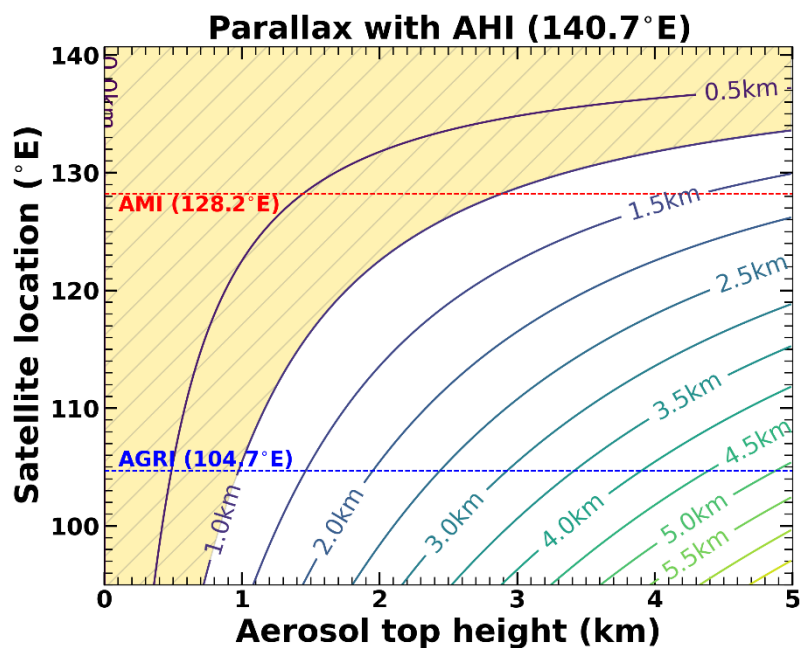
555 **Figure 3: Contour of theoretical parallax when one satellite in a pair is AHI and the other moves from 95° E to 140° E, according to the height of target aerosol layer. Yellow shading indicates parallax values that cannot be resolved using 1 km resolution imagers.**
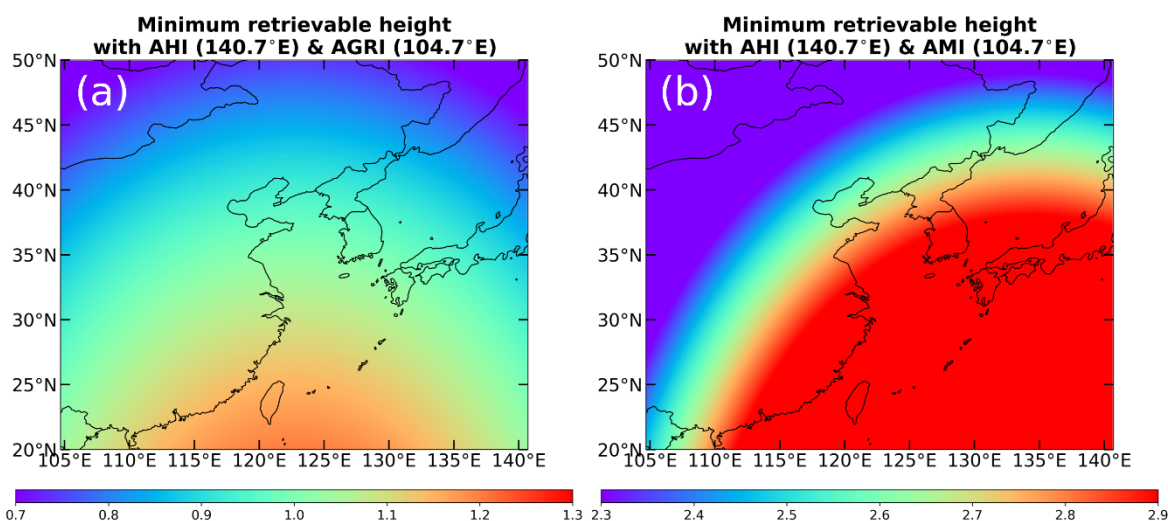
Figure 4: Minimum retrievable aerosol height from the (a) AHI–AGRI and (b) AHI–AMI (b) satellite pairs. The 560 **minimum retrievable height is set for 1 km resolution images to resolve parallax.**
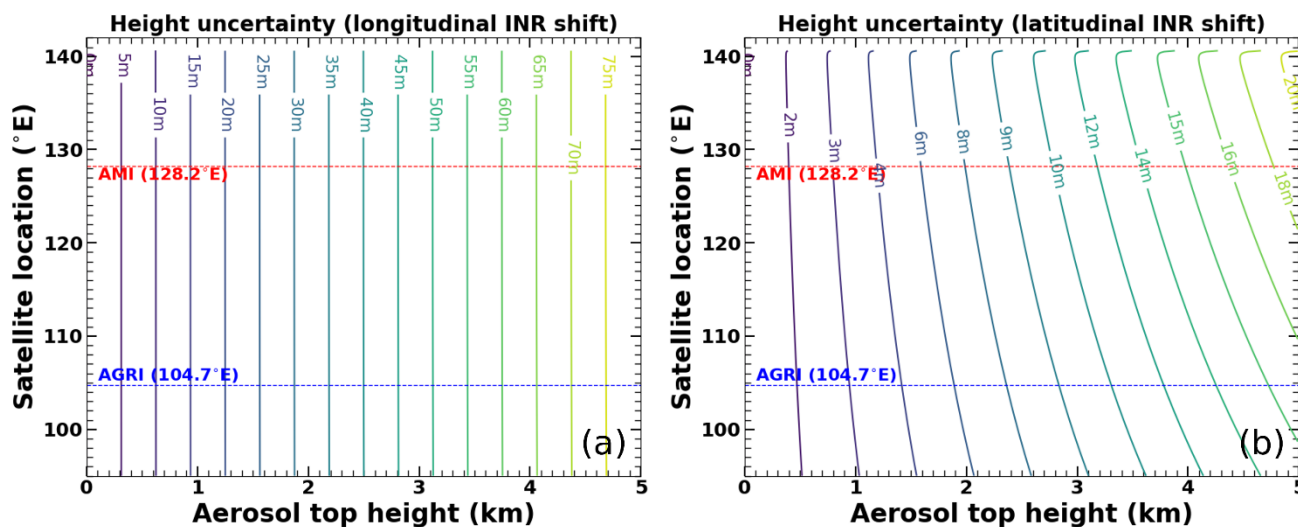
Figure 5: Height retrieval uncertainty assuming 1 km latitudinal (a) and longitudinal (b) shifts in AHI geolocation.
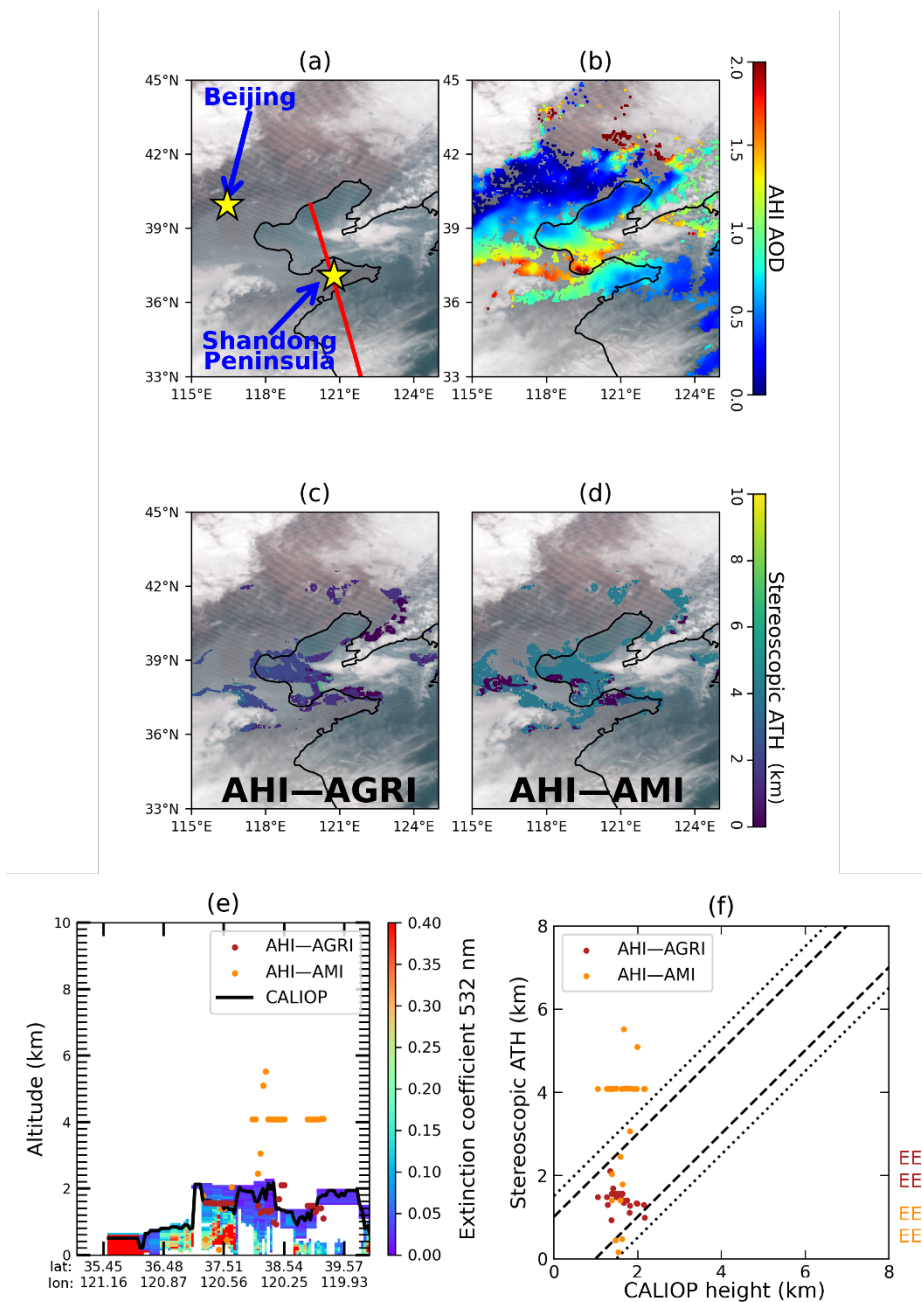
Figure 6: A case of ATH retrieval on 23 January 2020. (a) RGB image of the area of interest (red line shows CALIOP
overpass). (b) AHI AOD. (c) Stereoscopic ATH retrieved using AHI–AGRI. (d) Stereoscopic ATH retrieved using
AHI–AMI. (e) Stereoscopic ATH and CALIOP extinction coefficient profile (red dots represent ATH from AHI–
AGRI, orange dots from AHI–AMI, and black line represents CALIOP height). (f) Scatterplot of CALIOP height
versus stereoscopic ATH.
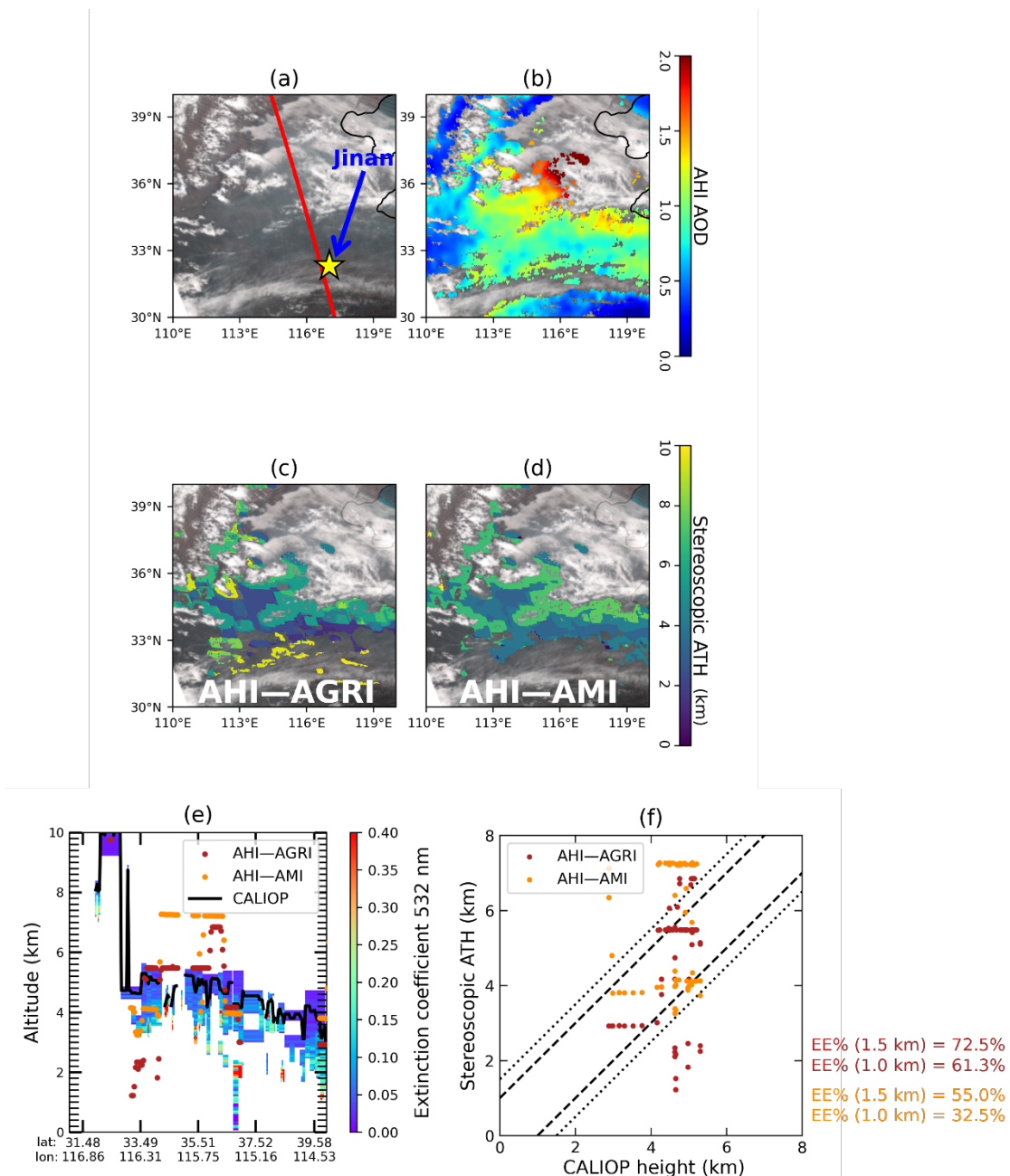
Figure 7: As for Fig. 6, but for 8 April 2020.
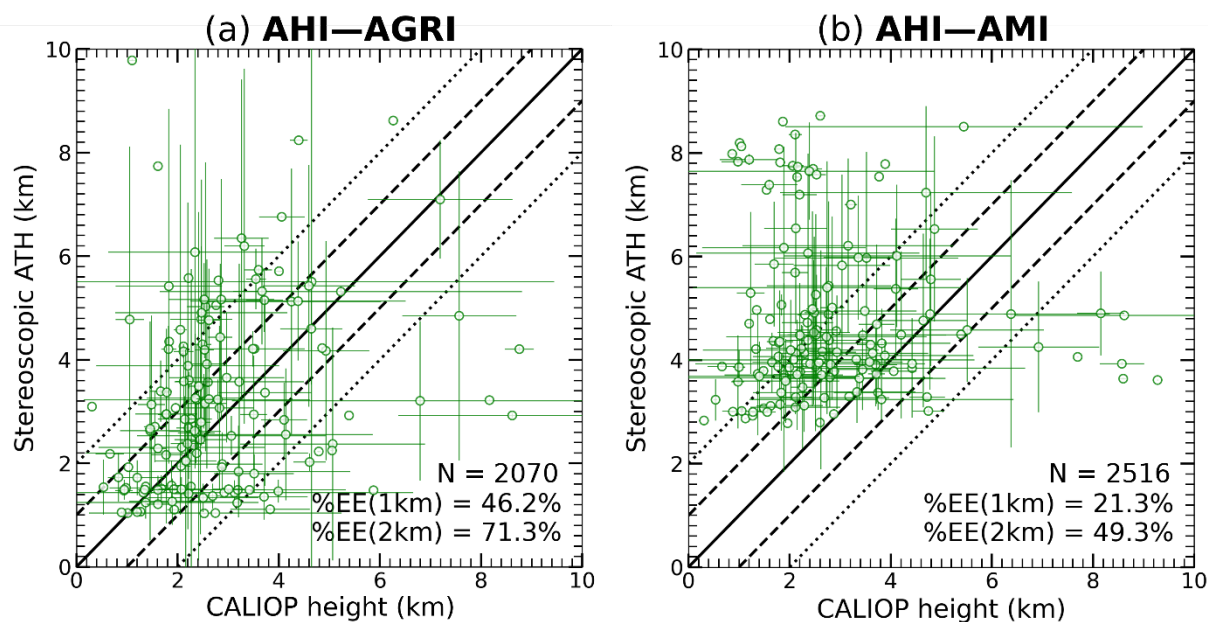
Figure 8: Scatterplots of scene-averaged CALIOP height versus stereoscopic ATH of the (a) AHI–AGRI and (b) AHI–AMI satellite pairs.
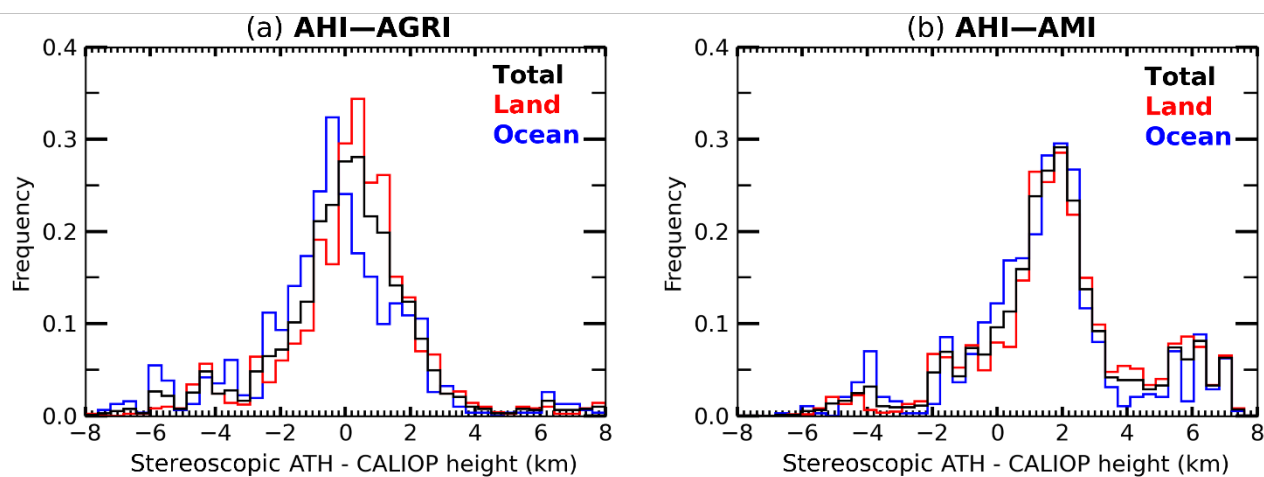
575 **Figure 9: Frequency distributions of the difference between stereoscopic ATH for the (a) AHI–AGRI and (b) AHI–AMI satellite pairs and CALIOP height.**
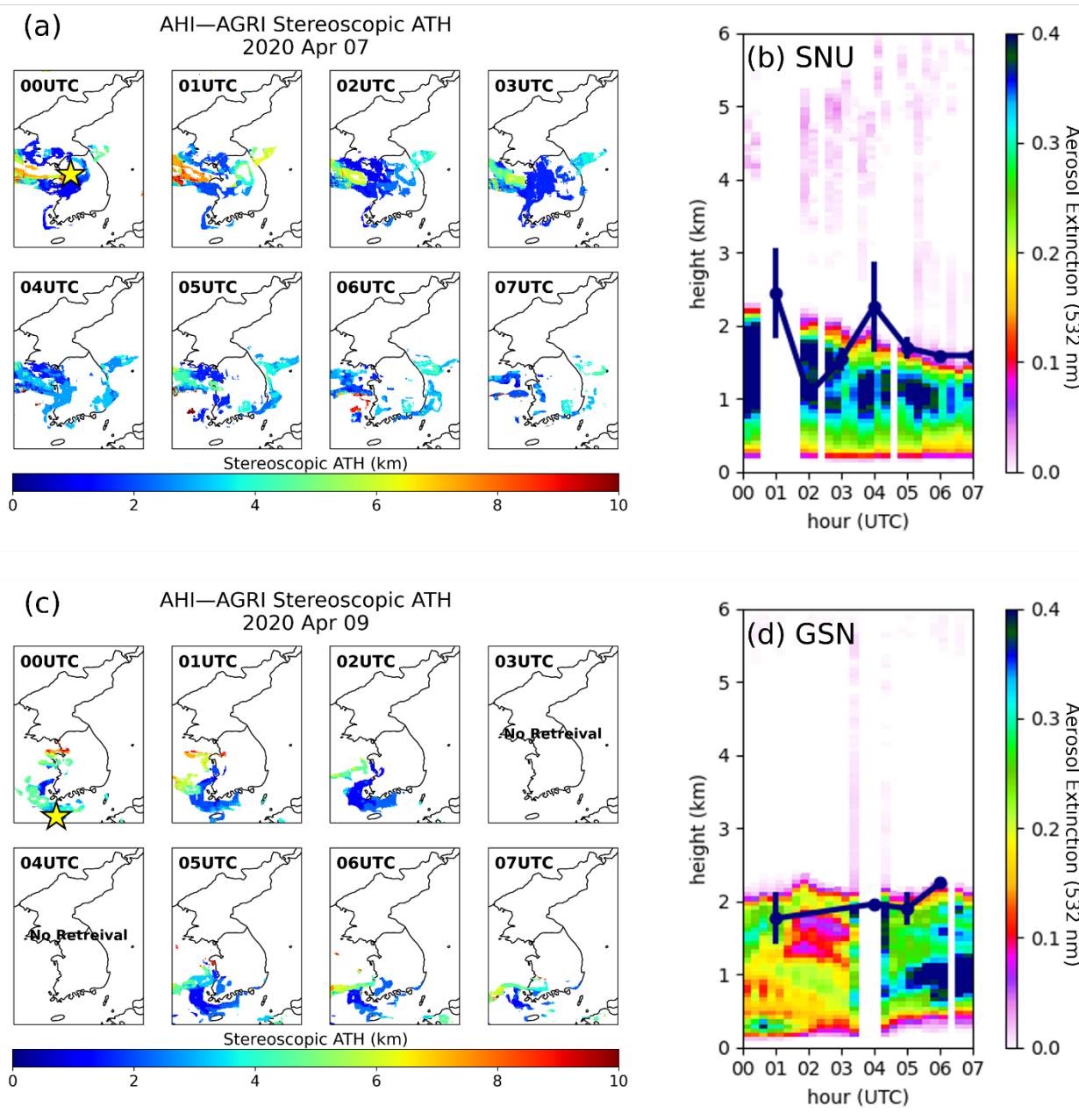
Figure 10: (a) Hourly stereoscopic ATH maps for 7 April 2020. (b) Aerosol extinction profile observed at SNU on 7 April 2020. The navy line represents the ATH from AHI–AGRI. (c) As for (a), but for 9 April 2020. (d) As for (b), but for the GSN station. Yellow stars in (a) and (b) represents ground-based lidar stations at Seoul National University and Gosan, respectively.